Zhang *et al.*
Chinese Journal of Mechanical Engineering (2023) 36:137
https://doi.org/10.1186/s10033-023-00949-8

Chinese Journal of Mechanical Engineering

ORIGINAL ARTICLE

Open Access

Dynamic Investigations on the Wear Behavior of a 3D Revolute Joint Considering Time-Varying Contact Stiffness: Simulation and Experiment

Li Zhang[1], Yining Fang[2*], Guanghan Bai[2] and Junyong Tao[2]

Abstract

The existence of the relative radial and axial movements of a revolute joint's journal and bearing is widely known. The three-dimensional (3D) revolute joint model considers relative radial and axial clearances; therefore, the freedoms of motion and contact scenarios are more realistic than those of the two-dimensional model. This paper proposes a wear model that integrates the modeling of a 3D revolute clearance joint and the contact force and wear depth calculations. Time-varying contact stiffness is first considered in the contact force model. Also, a cycle-update wear depth calculation strategy is presented. A digital image correlation (DIC) non-contact measurement and a cylindricity test are conducted. The measurement results are compared with the numerical simulation, and the proposed model's correctness and the wear depth calculation strategy are verified. The results show that the wear amount distribution on the bearing's inner surface is uneven in the axial and radial directions due to the journal's stochastic oscillations. The maximum wear depth locates where at the bearing's edges the motion direction of the follower shifts. These findings help to seek the revolute joints' wear-prone parts and enhance their durability and reliability through improved design.

Keywords Multibody dynamics, 3D revolute joint, Wear prediction, Digital image correlation

1 Introduction

The linkage mechanism is widely applied in the industrial and aerospace fields, e.g., in robotic arms, excavators, and satellite antenna systems [1]. The revolute joints, which are composed of the journal and bearing between the linkages, are one of the mechanism's weak and vulnerable components [2, 3]. Degradations and failures in these revolute joints may lead to a decrease in accuracy, movement instability, vibrations, and noises [4]. Joint clearance is a main factor that influences the revolute joints' performance [5–8]. Existing works [9–15] have demonstrated that there are radial and axial clearances [i.e., three-dimensional (3D) clearance] in revolute joints between the journal and the bearing. Thus, this paper focuses on the 3D revolute joint with 3D clearance in a linkage mechanism.

Many researchers have investigated the dynamic characteristics of 3D revolute joints in mechanical systems. The mechanical systems' dynamic responses show significant nonlinearity and a loss of motion accuracy due to the presence of 3D clearances [16]. Flores et al. [9] pointed out that the motion in a 3D revolute joint is divided into 4 possible contact scenarios, namely

*Correspondence:
Yining Fang
fangyining@nudt.edu.cn
[1] College of Information and Communication, National University of Defense Technology, Wuhan 430010, China
[2] Laboratory of Science and Technology on Integrated Logistics Support, College of Intelligence Science and Technology, National University of Defense Technology, Changsha 410073, China

non-contact, single-point contact, line contact and two-point contact on different sides. Tian et al. [10] extended Flores et al.'s work as they considered the effects of rod flexibility and joint lubrication. Liu et al. [11] discussed the effects of multiple 3D clearances on the dynamic behavior and adjusted the motion accuracy of the rigid-flexible coupled multibody system via a feedback control scheme. However, the influences of wear on the system dynamic performance in 3D revolute joints are still unknown.

Wear is a common failure mode in mechanical systems [17]. It is generally catalyzed by lubrication conditions, applied load, and material properties. Revolute joint wear involves the intercoupling of the parts' various motion states at the system level [18]. The clearance in the 3D revolute joint continues to expand and the profile of the contact surface between the journal and the bearing is strongly subject to wearing [12, 19]. The mechanical system's dynamic performance is then deteriorated by shocks and vibrations. In turn, the wearing procedure is accelerated under the spatial motion of the journal in the revolute joint [20].

Arhcard's wear model is widely applied in wear calculation, which correlates the wear volume with some physical and geometrical properties of the contact pairs, such as contact force, sliding distance, and hardness [21]. Based on this model, Flores [17] considered the contact pairs' profile variation and established a numerical wear model to quantify and predict the wear depth in a revolute joint. Mukrus et al. [22, 23] studied the influence of joint clearance and wear in a slider-crank mechanism. Their results showed that the joint wear increased the joint contact force and accelerated the wear progress. Zhao et al. [24] investigated the effects of flexibility and clearance size on joint wear. They found that rod flexibility weakened the wear behavior while joint clearance aggravated the wear behavior. Bai et al. [25] and Xiang et al. [26] combined the dynamic analysis and wear procedure by using iterative approaches in mechanical systems. The results demonstrated that progressive deformation on the contact surface may arise due to wear. The contact stiffness changed with the curvature radius as an essential parameter in contact force calculation [27]. Yang [28] investigated the time-varying contact stiffness between the journal and bearing in joints based on fractal geometry. Sun et al. [29] proposed a contact stiffness calculation model of joint surfaces that considered critical deformation change. Further considering the deformation in contact areas, Xu et al. [18] built a revolute joint wear model with a discretized profile to carry out the numerical computation. However, the existing works did not unveil the effects of time-varying contact stiffness in studying revolute joints' wear behavior. Studying these effects may improve the understanding of the wear behavior and the wear prediction in the future.

To validate the dynamic performances in the numerical model, experiments are conducted on testing mechanisms. Most of the experimental methods fall into two categories: contact measurement and non-contact measurement. The accelerator measuring approach is a commonly used contact measurement. Xu et al. [18] and Wang et al. [30] employed accelerators to obtain motion signals in their slider-crank mechanisms. Notably, these accelerators were installed on several limited testing points and they may pose extra masses on the operative bodies. The digital image correlation (DIC) method is a typical non-contact measurement approach that utilizes industrial cameras to photograph the objects with preset speckles, and then analyzes the obtained pictures' relevance as relative to the original pictures [31–33]. Compared with the accelerator measuring approach, the DIC method has the advantage of obtaining displacement and vibration information in the full field instead of at just several points. It is widely adopted in scenarios such as motion tracking, stress-strain measurement, and has good versatility and high measurement accuracy. In this study, the motion information of linkages is measured via the DIC method and then compared with the numerical calculation results to verify the proposed model.

Hence, a wear model integrating the modeling of a 3D revolute clearance joint, and the contact force and wear depth calculations is proposed in this paper. A contact force calculation formula is improved by taking into account the time-varying and nonlinear contact stiffness. A cycle-update wear depth calculation strategy is presented based on Archard's wear model [24]. To capture the connecting rods' motion state, the DIC method is applied in the experimental part. This study on the wear process in a revolute joint with radial and axial clearances will provide an appropriate way for the manufacturer to improve the joint structure's design. It will further enhance the revolute joints' durability and reliability.

This paper aims to investigate the effects of wear on the dynamic characteristics of a 3D revolute clearance joint and predict the distribution of wear on the bearing's inner surface. Section 1 introduces the current researches on the effects of clearance and wear on the dynamic characteristics of the 3D revolute joint. Then, Section 2 describes the features of the 3D clearance joint and establishes a contact force model considering time-varying contact stiffness. Section 3 studies a four-bar mechanism with a 3D revolute clearance joint while a numerical example and the simulation results are discussed. To verify the correctness of the wear model and

numerical calculations, a wear test along with the DIC measurement and a cylindricity test is carried out in Section 4. Finally, conclusions are given in Section 5.

2 Numerical Model of the 3D Revolute Joint with Clearance

Revolute joints are widely applied in industrial production, aerospace devices, and other mechanical products. They have high requirements for motion accuracy and reliability [15]. Early researches usually idealized the revolute joint's structure without clearance between the journal and the bearing for force and movement transmission [3]. However, this assumption ignores the clearance caused by assembly tolerance, manufacturing error, wear, etc. Given this, many literatures have studied the wear behavior of the revolute joints that have clearances, but most of them are confined to 2D planar mechanisms, and the influence of the journal's axial movement on the wear behavior is not fully considered [2, 5, 7, 21, 23, 26, 30, 34–51].

Due to the 3D clearance [9], the journal in the revolute joint has both radial and axial freedoms of motion. The centric lines of the journal and the bearing are not always parallel, thus creating considerable complexity and uncertainty to the joint's wear behavior. In this section, the geometrical characteristics of the 3D clearance joint are described in Section 2.1 and its dynamic mathematical expression is established in Section 2.2.

2.1 Geometrical Description for the 3D Revolute Joint

In this section, a 3D revolute clearance joint model is developed in reference to the model reported in Ref. [18]. Radial and axial clearances are considered in our model. The global coordinate $\boldsymbol{s}_b^{\text{global}}$ of discretized points on the bearing inner surface is obtained by Eq. (3), which can be applied in dynamic analysis. Figure 1 shows the discretizing procedure of the bearing inner surface. Figure 2 presents the contact force vectors and the profile-updating process considering wear.

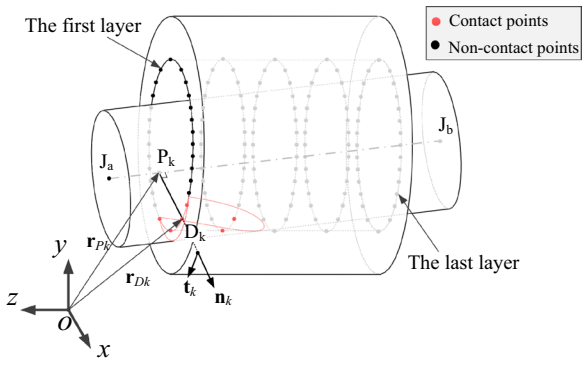

Figure 1 Schematic diagram of the discretized contact surface in a 3D revolute joint

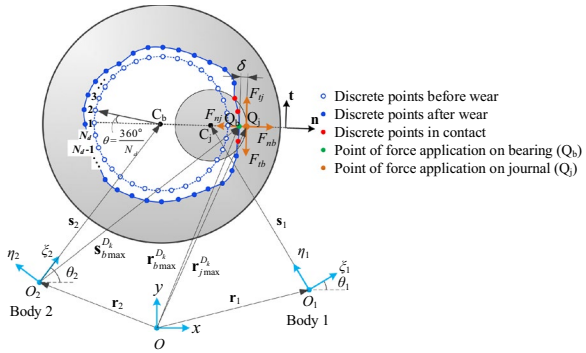

Figure 2 Discrete points in the first layer of the bearing on the inner surface

The revolute joint consists of 2 parts: the journal and bearing. The bearing provides position constraints for the journal's movement. According to the relative position of the journal and the bearing, the movement state is divided into four modes [9]: single-point contact, two-point contact, line contact, and free flight. In most cases, the journal and the bearing are in contact with each other, and thus friction and wear will occur. The wear is the main source of shock, vibration, noise, and failure in the life cycle of mechanical equipment. Therefore, establishing the constraint equation of motion is a prerequisite when studying the motion feature of the joint structure under the effects of wear and clearance.

Figure 1 presents a schematic of a 3D revolute clearance joint in one-side contact mode. The journal is a rigid body, and the revolute joint is not lubricated. In this study, we assume that the bearing in the 3D revolute joint is soft and deformable, while the journal is hard and non-deformable [18]. When contact and collision occur in a 3D revolute clearance joint, the contact surface's profile on the bearing changes, while the journal surface's profile does not. For a detailed investigation of the wear depth and distribution, the inner surface of the bearing is discretized into N_l layers and N_d points per layer. N_l represents the number of discretized layers and N_d represents the number of discretized points per layer. The layers and points are spaced at equal intervals on the bearing inner surface.

The red dots represent the contact points on the inner surface, while the black dots represent the non-contact points. D_k is a point on the bearing's inner surface, and P_k is the perpendicular foot of segments $\overline{P_kD_k}$ and $\overline{J_aJ_b}$. The normal vector of the contact force at point D_k is expressed as:

$$\boldsymbol{n}_k = \frac{\boldsymbol{r}_{Dk} - \boldsymbol{r}_{Pk}}{\|\boldsymbol{r}_{Dk} - \boldsymbol{r}_{Pk}\|}, k = 1, 2, \cdots, N, \tag{1}$$

where $\boldsymbol{r}_{Dk}$ is the vector line connecting the origin of the coordinates O and point D_k, $\boldsymbol{r}_{Pk}$ is the vector line connecting the origin of the coordinates O and point P_k, and N is the total number of discretized points on the bearing's inner surface ($N = N_l \times N_d$). Thus, $\boldsymbol{t}_k$ is derived by rotating $\boldsymbol{n}_k$ by 90° in the clockwise direction.

As shown in Figure 2, the first circular layer of the bearing's inner surface is discretized into N_d points, beginning at the negative x-axis and rotating clockwise at θ intervals. xOy is the global reference coordinates, while $\xi_1 O_1 \eta_1$ and $\xi_2 O_2 \eta_2$ are the local reference coordinates of body 1 and body 2, respectively. The contact force and contact points are also depicted in Figure 2. Considering the wear depth, the local coordinates of these discrete points referring to point D are calculated as:

$$\boldsymbol{s}_b^{\text{local}} = \boldsymbol{C}_b + \begin{bmatrix} -(R_b + h(t)) \cdot \cos\left((m-1) \cdot \frac{360^\circ}{N_d}\right) \\ (R_b + h(t)) \cdot \sin\left(m \cdot \frac{360^\circ}{N_d}\right) \\ w_b/2 - (n-1) \cdot w_b/(N_l - 1) \end{bmatrix}, m = 1, 2, \cdots, N_d; n = 1, 2, \cdots, N_l, \tag{2}$$

where $\boldsymbol{C}_b$ denotes the coordinates of the bearing's geometrical center point, R_b is the initial radius of the bearing's inner surface, $h(t)$ is the wear depth of each discrete point, and w_b is the width of the bearing. The global coordinate vector of discrete points $\mathbf{s}_b^{\text{global}}$ is obtained by translating and rotating transformations from the local coordinate vector $\mathbf{s}_b^{\text{global}}$:

$$\begin{bmatrix} \boldsymbol{s}_b^{\text{global}} \\ 1 \end{bmatrix} = \boldsymbol{T} \cdot \boldsymbol{R}_x \cdot \boldsymbol{R}_z \cdot \boldsymbol{R}_y \cdot \boldsymbol{T}^{-1} \cdot \begin{bmatrix} \boldsymbol{s}_b^{\text{local}} \\ 1 \end{bmatrix}, \tag{3}$$

where $\boldsymbol{T}$ represents the translation matrix, and $\boldsymbol{R}_x$, $\boldsymbol{R}_y$, and $\boldsymbol{R}_z$ represent the conversion matrix rotating around the x, y, and z axes, respectively. These matrices are expressed as:

$$\mathbf{T} = \begin{bmatrix} 1 & 0 & 0 & x_D \\ 0 & 1 & 0 & y_D \\ 0 & 0 & 1 & z_D \\ 0 & 0 & 0 & 1 \end{bmatrix} \quad \boldsymbol{R}_x = \begin{bmatrix} 1 & 0 & 0 & 0 \\ 0 & \cos\theta_x & \sin\theta_x & 0 \\ 0 & -\sin\theta_x & \cos\theta_x & 0 \\ 0 & 0 & 0 & 1 \end{bmatrix}$$
$$\boldsymbol{R}_y = \begin{bmatrix} \cos\theta_y & 0 & -\sin\theta_y & 0 \\ 0 & 1 & 0 & 0 \\ \sin\theta_y & 0 & \cos\theta_y & 0 \\ 0 & 0 & 0 & 1 \end{bmatrix} \quad \boldsymbol{R}_z = \begin{bmatrix} \cos\theta_z & \sin\theta_z & 0 & 0 \\ -\sin\theta_z & \cos\theta_z & 0 & 0 \\ 0 & 0 & 1 & 0 \\ 0 & 0 & 0 & 1 \end{bmatrix}, \tag{4}$$

Since the clearance in revolute joints is very small compared to the geometrical size of multibody systems, the penetration depth is approximately considered as [20]:

$$\delta = e - c, \tag{5}$$

where e is the distance between the centroids of the journal and the bearing in the xoy plane and c is the initial joint clearance.

2.2 Normal and Tangential Contact Force Models

This section presents the normal and tangential contact force models. An improved normal contact force model that considers time-varying contact stiffness is proposed in Eqs. (8)–(10). The contact forces and moments on bearing and journal are derived in Eqs. (15)–(17).

The contact force model plays an essential role in dynamic analysis for multibody systems. The continuous contact force model treats the penetration depth as an index to measure the degree of the contact area's deformation and calculate the value of the contact force [52]. The size and location of the penetration depth under various contact modes are different. It has a corresponding impact on the multibody system's dynamic responses.

Hertz's pioneer work focused on the impact process of two elastic bodies, but Hertz Law does not take into account energy dissipation [53]. Considering energy dissipation, the Lankarani–Nikravesh (L–N) model [53] is widely used to calculate the contact force in multibody systems. This model is written as:

$$F_n = K\delta_{\max}^n \left[1 + \frac{3(1 - c_e^2)\dot{\delta}}{4\dot{\delta}^{(-)}}\right], \tag{6}$$

where K is contact stiffness; δ is the relative penetration depth; $\delta_{\max}$ is the maximum penetration depth; $\dot{\delta}$ is the relative velocity of penetration; $\dot{\delta}^{(-)}$ is the initial velocity

of penetration; n is the exponent value, which is set to 1.5 for most metal contacts [18]; and c_e is the restitution coefficient, which is set to 0.9 in this study. The contact stiffness K is calculated as follows:

$$\begin{aligned} K &= \frac{4}{3\pi\left(h_j + h_b\right)}\left(\frac{R_j R_b}{R_b - R_j}\right)^{\frac{1}{2}}, \\ h_m &= \frac{1-\nu_m^2}{\pi E_m}(m = j, b). \end{aligned} \tag{7}$$

In the above equation, E_m is the Yang's modulus; ν_m is the Poisson's ratio; subscripts j and b indicate the journal and bearing, respectively; R_j is journal radius; and R_b is the radius of the bearing's inner surface.

where R_b denotes the initial radius of the bearing's inner surface, and $h(t)$ denotes the wear depth at contact area at time t, which is calculated using Eq. (20).

The tangential contact force is calculated as follows:

$$F_t = \mu F_n, \tag{11}$$

where μ is the friction coefficient of the contact surfaces.

The tangential contact force in revolute joints is generally calculated using Coulomb's friction law. However, this law does not consider the relative tangential slip velocity, and the calculation using this law may become complex owing to its obvious nonlinear properties during the switch between sticking and sliding conditions [26]. To prevent sudden changes in the tangential friction force, the relationship between the friction coefficient and the relative tangential velocity is modified as follows:

$$\mu = \begin{cases} \mu_d, & |V| > V_d, \\ \mu_s \sin\left(\frac{\pi}{2}\frac{|V|}{V_s}\right), & |V| < V_s, \\ \frac{\mu_s + \mu_d}{2} + \frac{1}{2}\left[(\mu_s - \mu_d)\cos\left(\pi\frac{|V| - V_s}{V_d - V_s}\right)\right], & V_s \le |V| \le V_d, \end{cases} \tag{12}$$

In this study, a modified L–N contact force model is proposed to calculate the normal contact force in the 3D revolute joint. The main difference from the original contact force model is the use of a time-varying contact stiffness $K(t)$ that considers the wear depth on the bearing's inner surface; the original model includes a constant generalized contact stiffness K that considers the initial radius values of the journal and bearing. In the modified L–N contact force model, contact force in the normal direction is calculated as follows:

$$F_n = K(t)\delta_{\max}^n\left[1 + \frac{3\left(1 - c_e^2\right)\dot{\delta}}{4\dot{\delta}^{(-)}}\right]. \tag{8}$$

The continuously updating contact stiffness $K(t)$ is calculated as follows:

$$\begin{aligned} K(t) &= \frac{4}{3\pi\left(h_j + h_b\right)}\left(\frac{R_j R_b(t)}{R_b - R_j}\right)^{\frac{1}{2}}, \\ h_m &= \frac{1-\nu_m^2}{\pi E_m}\left(m = j, b\right), \end{aligned} \tag{9}$$

where $R_b(t)$ is the latest update of the contact region's radius on the inner surface of bearing considering wear depth, which can be calculated as:

$$R_b(t) = R_b + h(t), \tag{10}$$

where V is the tangential relative velocity, V_d is the switching velocity between static and sliding friction conditions, V_s is the switching velocity between the stick and slip conditions, and μ_d and μ_s represent the sliding and static friction coefficients, respectively.

The contact force on the bearing at point D_k is calculated as follows:

$$\boldsymbol{F}_b^k = \begin{bmatrix} F_{bk}^x \\ F_{bk}^y \\ F_{bk}^z \end{bmatrix}^{\mathrm{T}} = f_{bk}^n \boldsymbol{n}_k + f_{bk}^t \boldsymbol{t}_k, f_{bk}^n = F_n^k, f_{bk}^t = F_t^k. \tag{13}$$

Similarly, the contact force on the journal is calculated as follows:

$$\boldsymbol{F}_j^k = \begin{bmatrix} F_{jk}^x \\ F_{jk}^y \\ F_{jk}^z \end{bmatrix}^{\mathrm{T}} = f_{jk}^n \boldsymbol{n}_k + f_{jk}^t \boldsymbol{t}_k, f_{jk}^n = -F_n^k, f_{jk}^t = -F_t^k. \tag{14}$$

Note that the contact forces at those points in the non-contact mode are zero vectors because their penetration depths are equal to zero. Therefore, the resultant force on the bearing is:

$$\boldsymbol{F}_b = \sum_{k=1}^{N} \boldsymbol{F}_b^k, \boldsymbol{F}_j = -\boldsymbol{F}_b. \tag{15}$$

The moments generated due to the contact force and gravity are expressed as follows:

$$\boldsymbol{T}_b = \sum_{k=1}^{N} \boldsymbol{F}_b^k \times \boldsymbol{r}_b^k + \boldsymbol{G}_b \times \boldsymbol{r}_{bG}, \tag{16}$$

$$\boldsymbol{T}_j = \sum_{k=1}^{N} \boldsymbol{F}_j^k \times \boldsymbol{r}_j^k + \boldsymbol{G}_j \times \boldsymbol{r}_{jG}, \tag{17}$$

where $\boldsymbol{F}_{\mathrm{b}}^{\mathrm{k}}$ and $\boldsymbol{F}_{\mathrm{j}}^{\mathrm{k}}$ are calculated using Eq. (13) and Eq. (14), respectively; $\boldsymbol{r}_{\mathrm{b}}^{\mathrm{k}}$ denotes the vector from the kth discrete point to its rotating point on rigid body b; $\boldsymbol{r}_{\mathrm{j}}^{\mathrm{k}}$ denotes the vector from the perpendicular foot on the journal of the kth discrete point to its rotating point on rigid body j; $\boldsymbol{r}_{\mathrm{bG}}$ and $\boldsymbol{r}_{\mathrm{jG}}$ denote the vectors from the centroid of rigid bodies b and j to their rotating points, respectively; and $\boldsymbol{G}_b$ and $\boldsymbol{G}_j$ denote the gravities of rigid bodies b and j, respectively.

2.3 Wear Model

Generally, the joint wear in multibody systems is based on Archard's model [38], which is expressed as:

$$\frac{V_w}{s} = k_w F_n, \tag{18}$$

where V_w is the wear volume, s is the relative sliding distance, k_w is the wear coefficient, and F_n is the contact force in the normal direction calculated by Eq. (8).

Because this model is applied for iteration, its differential form is used:

$$\frac{\mathrm{d}h}{\mathrm{d}s} = k_w P, \tag{19}$$

where h is the wear depth, and P is the contact pressure.

Furthermore, because the variables in this model are discrete, when using the recursion approach, the difference form is applied in the wear analysis as follows:

$$h(t) = h(t-1) + k_w \cdot \frac{F_n \cdot \Delta s(t)}{A(t)}, \tag{20}$$

where $h(t)$ is the wear depth at time t, $h(t-1)$ is the wear depth at the previous step, F_n is the normal contact force calculated by Eq. (8), $\Delta s(t)$ is the incremental value of the sliding distance, and $A(t)$ is the contact area derived from the numbers of discrete contact points in each computational recursion.

2.4 Integrated Method of Dynamic Analysis and Wear Process

Mechanical system's dynamic characteristics and the wear of the revolute clearance joint couple with each other and create effects mutually over time [6]. This section integrates the dynamic calculation process of the mechanical system with the wear calculation process, calculates the force and motion parameters in each calculation cycle, and then updates the bearing contact surface profile for the next cycle after obtaining the wear distribution. Due to the discretization of the bearing's internal surface, some contact force curves with "pseudo high frequency" may be generated during calculation [18].

Figure 3 depicts an integrated approach of dynamics and wear. Firstly, according to the geometric information and material parameters of each the mechanical system's parts, the geometric model (including initial parameters $\boldsymbol{q}_0$, $\dot{\boldsymbol{q}}_0$) is established for kinematics and dynamics analysis. The discretization process of the contact surface of the bearing in the revolute clearance joint was introduced in Section 2.1, in which the geometric characteristics of the journal and the bearing are regarded as the initial state.

Then, the differential equation of system motion is established according to the force condition. Because the system's linkages are all taken as rigid structures, the motion parameters of markers such as the centroid and the geometric center can be reckoned through the positions of several key points when calculating displacement information. Specifically, the ode15s function is used in the MATLAB software to solve high-order equations of motion, and the solving step size is self-adaptive and continuously adjusted [18]. The position $\boldsymbol{q}$ at time t is the output to the next step.

Based on the position $\boldsymbol{q}$, the force conditions of the journal and the bearing of the revolute clearance joint are obtained considering a time-varying contact stiffness $K(t)$. With the relative position of the bearing and journal, the search algorithm checks the regional contact area and distribution. The relative slip distance, penetration depth, contact area, and other key parameters are substituted into Archard's model to calculate the wear amount of the contact part in a time segment. In this part, normal contact force F_n and tangential contact force F_t are also exported.

At last, based on the initial geometry and position characteristics of the revolute clearance joint, the geometric contour of the bearing's inner surface is updated for the

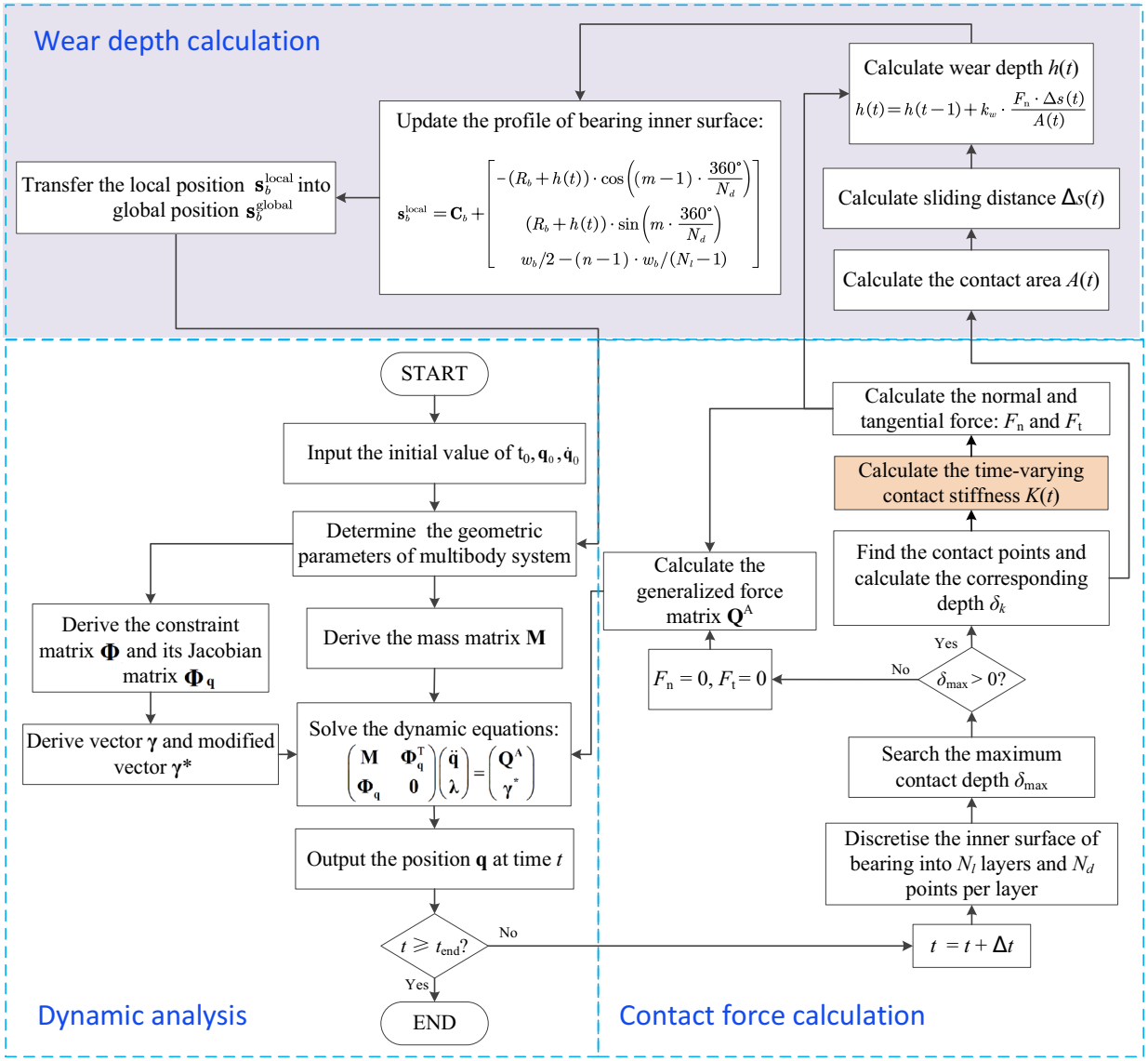

Figure 3 Flowchart for wear prediction and analysis procedures in multibody systems with a 3D revolute joint

next calculation cycle by integrating the wear information of each contact part of the bearing's inner surface. It is a cycle-update wear depth calculation strategy put forward in literature [54]. After several calculation cycles, the wear distribution data of the bearing inner surface of the revolute clearance joint and the curves of kinematics and dynamic parameters with the time spent in each calculation cycle are output.

3 Numerical Example and Result Analysis

In this section, the nonlinear dynamic behavior of a spatial four-bar mechanism with a 3D revolute joint are investigated. The four-bar mechanism with a 3D revolute joint that considers wear is modelled in Section 3.1. Then, the wear depth distribution and its effects on the system's dynamic performances are discussed in Section 3.2.

3.1 A Four-bar Mechanism with a 3D Revolute Joint that Considers Wear

This section aims to develop the dynamic equations of a four-bar mechanism [55], which is a typical structure with a 3D revolute joint in studying the system's dynamic response. The geometrically schematic diagram (see Figure 4) and detailed parameters (see Tables 1 and 2) about the four-bar mechanism are presented as follows. Then, dynamic equations are formulated to calculate contact forces and position information in Eq. (27).

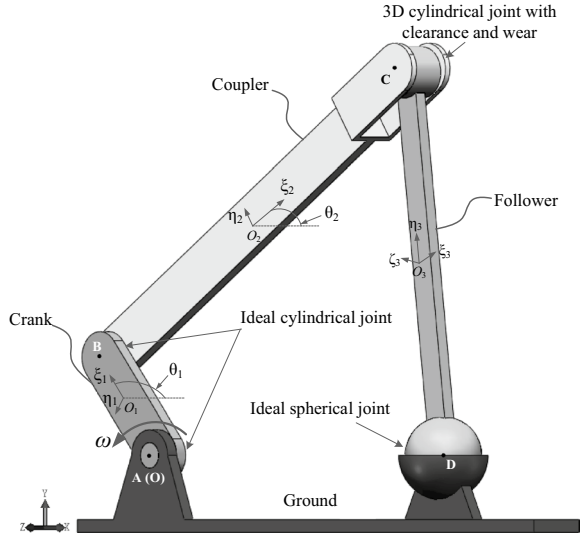

Figure 4 Geometric features of the four-bar mechanism model

Table 1 Inertial and geometrical properties of the four-bar mechanism model

Part name	Length (m)	Mass (kg)	Moment of inertia (kg·m^2)
Crank	0.10	0.46	I_1=0.0019
Coupler	0.40	1.45	I_2 = 0.0927
Follower	0.30	1.50	$\begin{bmatrix} I_{3x}=0.0317 & & \\ & I_{3y}=0.0004 & \\ & & I_{3z}=0.0317 \end{bmatrix}$
Ground	0.30	–	–

The geometric features of the spatial four-bar mechanism model are shown in Figure 4, including ground support, crank, coupler, and follower. The ground support is fixed entirely in the global coordinates. The driving moment is applied to the crank with a constant revolving speed of 120 r/min. The joints between the ground and crank (joint A), crank and coupler (joint B), and follower and ground (joint D) are considered ideal, i.e., clearance and friction are ignored. Particularly, a perfect ball joint is applied in joint D to allow the bearing in joint C to move in spatial directions. In contrast, joint C is considered an imperfect joint, i.e., clearance and friction are considered. Table 1 presents the geometrical parameters of the spatial four-bar mechanism [55], and Table 2 presents the mechanical properties and parameters considered in the dynamic analysis [18].

The generalized coordinates $\boldsymbol{q}$ of the multibody system are expressed as follows:

$$\boldsymbol{q} = \left[x_1, y_1, \theta_1, x_2, y_2, \theta_2, x_3, y_3, z_3, \theta_{3x}, \theta_{3y}, \theta_{3z}\right]^{\mathrm{T}}, \quad (21)$$

where (x_1, y_1, 0), (x_2, y_2, 0), and (x_3, y_3, z_3) denote the global coordinate values of the mass center in the crank (O_1), coupler (O_2), and follower (O_3), respectively. θ_1 and θ_2 are the rotation angles of the crank and coupler relative to the x-direction, respectively. Meanwhile, θ_{3x}, θ_{3y}, and θ_{3z} are the angles of discrete points on the follower rotating around the positive x, y, and z axes at point D, respectively.

Table 2 Parameters considered in the dynamic analysis and wear prediction of the 3D joint with clearance

Parameter	Value
Journal diameter	15 mm
Bearing diameter	16 mm
Length of journal and bearing	17 mm, 15 mm
Initial radial and axial clearance of joint	0.5 mm, 1 mm
Stick–slip switching velocity v_s and static–sliding friction switching velocity v_d	1 mm/s, 10 mm/s
Young's modulus and Poisson's ratio of journal material (steel)	207 GPa, 0.29
Young's modulus and Poisson's ratio of bearing material (brass)	100 GPa, 0.39
Coefficient of restitution	0.9
Static and sliding coefficient of frictions	0.2, 0.1
Coefficient of wear	5.05×10^{-10} m^3/N·m
Number of layers of the discrete points on the bearing's inner surface	20
Number of the discrete points per layer on the bearing's inner surface	200
Crank rotation speed	120 r/min (counter-clockwise)
Integration method for solving dynamic equations	ode15s function in MATLAB
Baumgarte stability control parameters	α = 1000, β = 1000

The constraint equations involving the multibody system's kinematic and dynamic constraints are expressed as:

$$\boldsymbol{\Phi} = \begin{bmatrix} x_1 - \frac{L_1}{2}\cos\theta_1 \\ y_1 - \frac{L_1}{2}\sin\theta_1 \\ x_2 - 2x_1 - \frac{L_2}{2}\cos\theta_2 \\ y_2 - 2y_1 - \frac{L_2}{2}\sin\theta_2 \\ x_3 - L_4 - \frac{L_3}{2}\sin\theta_{3z} \\ y_3 - \frac{L_3}{2}\cos\theta_{3z}\cdot\cos\theta_{3x} \\ z_3 - \frac{L_3}{2}\cos\theta_{3z}\cdot\sin\theta_{3x} \\ \theta_1 - \theta_{10} - \omega t \end{bmatrix} = \mathbf{0}, \tag{22}$$

where L_1, L_2, L_3, and L_4 are the length of the crank, coupler, follower, and equivalent rod on the ground, respectively. θ_{10} is the initial value of θ_1, and ω is the rotation velocity of the crank in the counter-clockwise direction.

The vector $\boldsymbol{\gamma}$ in the dynamic equations is calculated as follows:

$$\boldsymbol{\gamma} = -\left(\boldsymbol{\Phi}_q\dot{\boldsymbol{q}}\right)_q\dot{\boldsymbol{q}} - \boldsymbol{\Phi}_{tt} - 2\boldsymbol{\Phi}_{qt}\dot{\boldsymbol{q}}, \tag{23}$$

where $\boldsymbol{\Phi}_q$ is the derivative of the Jacobian matrix with respect to $\boldsymbol{q}$, $\boldsymbol{\Phi}_{tt}$ is the second derivative of $\boldsymbol{\Phi}$ with respect to t, and $\boldsymbol{\Phi}_{qt}$ is the derivative of $\boldsymbol{\Phi}_q$ with respect to t.

To avoid constraint violations in the numerical calculations, the Baumgarte stabilization approach [56] is applied in the dynamic equations. Therefore, the vector $\boldsymbol{\gamma}$ was modified as:

$$\boldsymbol{\gamma}^* = \boldsymbol{\gamma} - 2\alpha\left(\boldsymbol{\Phi}_q\dot{\boldsymbol{q}} + \boldsymbol{\Phi}_t\right) - \beta^2\cdot\boldsymbol{\Phi}, \tag{24}$$

where α and β are the Baumgarte stabilization coefficients used as feedback control variables of the constraint violations in positions and velocities, respectively. They are experiential variables and generally determined by tens of trials.

The mass and inertia moments matrix of the four-bar mechanism is expressed as follows:

$$\boldsymbol{M} = \mathrm{diag}\left[\, m_1\ m_1\ I_1\ m_2\ m_2\ I_2\ m_3\ m_3\ m_3\ I_{3x}\ I_{3y}\ I_{3z}\,\right], \tag{25}$$

where m_1, m_2, and m_3 are the masses of the crank, coupler, and follower, respectively; I_1 and I_2 are the inertia moments of the crank and coupler with respect to the z-axis, respectively; I_{3x}, I_{3y}, and I_{3z} are the corresponding inertia moments of the follower in the x, y, and z directions, respectively.

The generalized force vector $\boldsymbol{Q}^{\mathrm{A}}$ is expressed as:

$$\boldsymbol{Q}^{\mathrm{A}} = \left[\, 0 \quad -m_1 g \quad 0 \quad F_j^x \quad -m_2 g + F_j^y \quad T_j \quad F_b^x \quad -m_3 g + F_b^y \quad F_b^z \quad T_b^x \quad T_b^y \quad T_b^z \,\right], \tag{26}$$

where g is the gravitational acceleration, and the other terms involving force and moment are calculated using Eqs. (13) to (17).

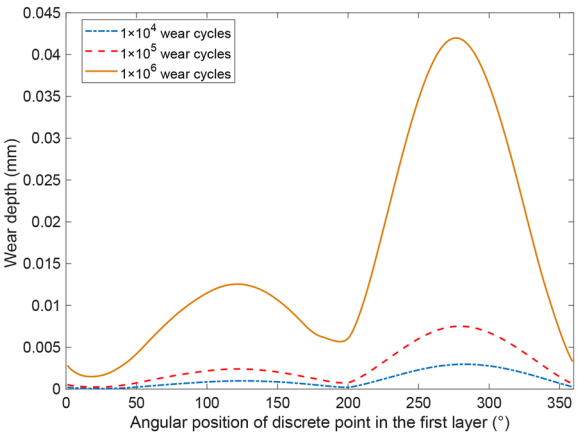

Figure 6 Wear depth of discrete points in the first layer at different angular positions

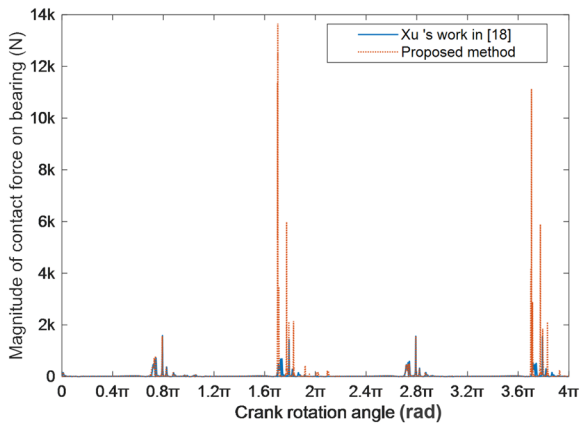

Figure 5 Magnitude of the contact force on the bearing

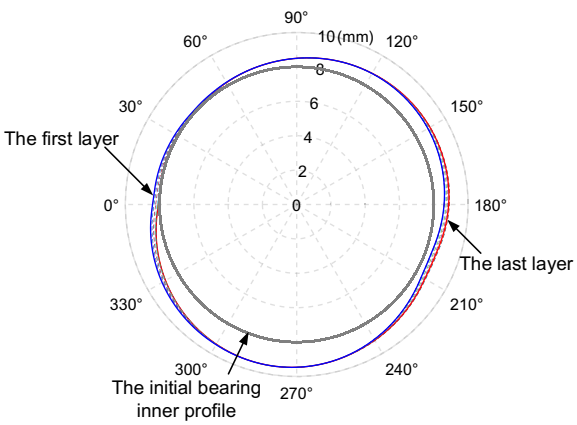

Figure 7 Wear depth distribution on the bearing's inner surface

The standard dynamic equation for a spatial multibody system is:

$$\begin{pmatrix} \boldsymbol{M} & \boldsymbol{\Phi}_q^{\mathrm{T}} \\ \boldsymbol{\Phi}_q & 0 \end{pmatrix} \begin{pmatrix} \ddot{\boldsymbol{q}} \\ \boldsymbol{\lambda} \end{pmatrix} = \begin{pmatrix} \boldsymbol{Q}^{\mathrm{A}} \\ \boldsymbol{\gamma}^{*} \end{pmatrix}. \tag{27}$$

In the above equation, $\boldsymbol{M}$ is the system mass and inertia moment matrix, $\boldsymbol{\Phi}_q$ is the Jacobian matrix of the kinematic constraints, $\ddot{\boldsymbol{q}}$ is the acceleration vector, $\boldsymbol{Q}^{\mathrm{A}}$ is the generalized force vector, $\boldsymbol{\gamma}^{*}$ is a modified vector obtained using the Baumgarte stabilization approach, and $\boldsymbol{\lambda}$ is the Lagrange multipliers vector, which is expressed as follows:

$$\boldsymbol{\lambda} = \begin{bmatrix} \lambda_1 & \lambda_2 & \cdots & \lambda_i \end{bmatrix}^{\mathrm{T}}, \tag{28}$$

where i is the number of constraint equations. In the four-bar mechanism model developed in this study, i is set as 8 because the amount of constraint equations in Eq. (22) is 8.

3.2 Results and Discussion

The simulation results in the four-bar mechanism are presented in this section. Specifically, the effects of the time-varying contact stiffness $K(t)$ and the wear depth distribution on the bearing are discussed. Figure 5 shows the magnitudes of contact forces in Xu's work [18] and the proposed model. Figure 6 shows the wear depth of discrete points in the first layer on different angular positions. Figure 7 shows the profiles of the bearing inner surface before and after wear (for 1×10^6 cycles).

The occurrence of wear in 3D revolute joints in multibody systems is a continuous, gradual, and long-term process [24, 38, 57, 58]. In this study, the profile of the bearing's inner surface is discretized into a certain number of independent nodes to simplify calculating the contact force. Further, these nodes are used to determine the contact area, calculate the depth of wear, and then update the contact profile.

In the L–N model, the generalized contact stiffness K is calculated using the initial radius values of the journal and bearing in a revolute joint. However, in the selected four-bar mechanism, the profile of the bearing's inner surface changes continuously due to wear. Accordingly, a time-varying contact stiffness $K(t)$ is adopted involving the wear depth on the bearing's inner surface. Compared with Xu's work [18] using constant contact stiffness K in Figure 5, the magnitude of the contact force in the proposed model shows the same trend at the start of a rotation period, but fluctuates more significantly in the end. The radius of the inner bearing surface increases after wear, leading to a larger clearance in the 3D revolute joint. As a result, strong shockwaves and vibrations are generated. Thus, the variation of the curvature radius of the worn surface in a revolute joint should be considered.

Figure 6 shows the wear depth of discrete points in the first layer on the bearing's inner surface at different angular positions from 1×10^4 to 1×10^6 wear cycles. When the number of wear cycles increases, the wear depth on the bearing and the wear speed tend to increase. The wear depth at different angular positions varies widely and reaches its maximum at around 280°. There are two peaks in each wear depth curve, which is consistent with the results obtained in previous studies [24, 26, 38]. The direction of the contact force and the location of the contact area determines this phenomenon.

Figure 7 shows the profiles of the bearing's inner surface before and after wear (for 1×10^6 cycles). The wear region is emphasized with a deformation scale factor to clearly show the relative wear depth. The closed lines in Figure 7 represent the angular positions of the discretized points from the first to the last layer. These profile lines have non-uniform shapes and are almost ellipses. A similar wear depth distribution in a 2D slider-crank mechanism was derived in a wear experiment conducted by Ref. [18]. Nevertheless, the measurement of the wear depth covers only one layer. Note that the closed curves of the first and last layers do not coincide completely. The results show that the two sides' wear depth on the bearing's inner surface is significantly different in the angular position owing to the translational and rotational motion between the central axes of the journal and bearing. This phenomenon is evident in 3D revolute joints, but does not occur in 2D revolute joints. The wear volume obtained in the 2D revolute joint represents the average value in the axial direction. Thus, the axial joint clearance's influence should be considered when studying the wear behaviour in multibody systems.

In summary, the change of the curvature radius of the bearing's inner surface that wear causes leads to a time-varying contact stiffness, which significantly influences the contact force in the dynamic analysis. Besides, the

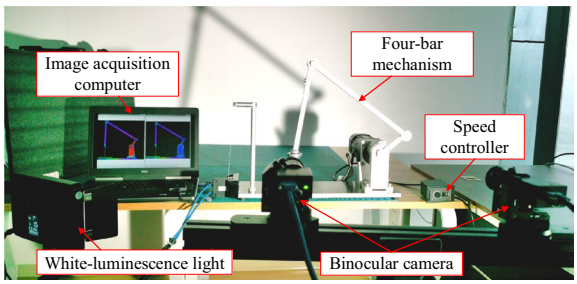

Figure 8 Test rig for dynamic performance measurement using DIC method

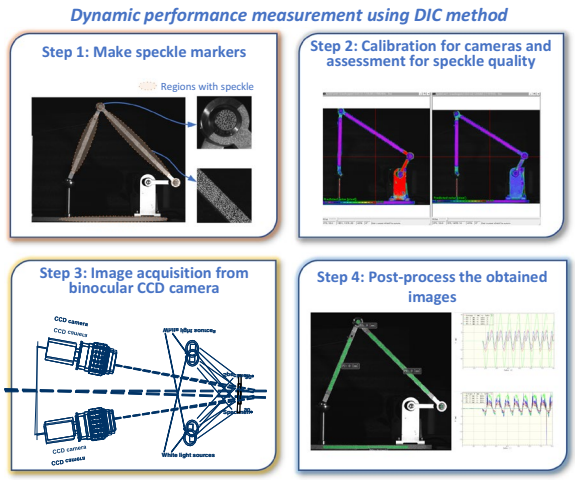

Figure 9 Procedure of dynamic performance measurement using the DIC method

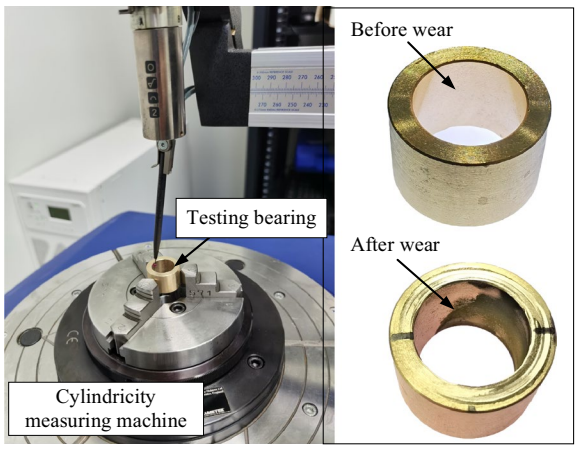

Figure 10 Cylindricity and contour measurement for bearing

Table 3 Experimental parameters in dynamic performance and contour measurement

Device	Parameter	Value
DIC device	Crank rotation speed	120 r/min
	Camera frame rate	50 fps
	Displacement measuring accuracy	3 μm
Cylindricity measuring machine	Roundness measurement accuracy	0.03 μm
	Number of layers along the axial direction	13
	Number of the measuring points per layer	18000

maximum wear depth locates at a specific region on the bearing edge.

4 Experimental Validation

In this section, the DIC measurement and cylindricity test are carried out to validate the effectiveness of the proposed model and the numerical algorithm. Compared with the accelerator measuring approach, the DIC method has the advantage of obtaining displacement and vibration information in the full field instead of at just several points. In Section 4.1, the test rig and measurement approaches are detailed and presented. Then, the experimental results are analyzed and discussed in Section 4.2.

4.1 Test Rig and Implement Procedure

To obtain the motion of the tested mechanism (see Figure 8), the DIC measurement method is adopted in this section. The measuring procedure is shown in Figure 9. The cylindricity of the inner surface of the worn bearing is measured in a cylindricity measuring machine (see Figure 10). The main experimental parameters are listed in Table 3. These parameters are in accordance with the simulation parameters in Section 3.1.

The test object is a four-bar mechanism with a 3D revolute joint. The spherical joint's function is to allow the journal in the revolute joint structure to produce a 3D motion in the bearing. This is the main feature that is different from the planar linkage mechanism, which makes the 3D movement of the revolute clearance joint more significant and is in line with the movement characteristics of mechanical equipment after wear. Similarly, Yan et al. [12] designed a special four-bar mechanism where the centric lines of the bearing and the journal were non-coincident and kept a preset angle in the initial state. However, the misalignment between the journal and the bearing is artificially manufactured and does not conform to the reality of the mechanism's movement process.

The four-bar test apparatus is composed of a low-carbon steel base, three aluminum-alloy supports, a driving motor, a reduction gearbox, a coupling, a crank, a connecting rod, a follower, a revolute clearance joint, and a spherical joint. The driving motor is a 120 W AC asynchronous motor with a speed controller. During the test, the crank's rotation speed is constantly 120 r/min. The crank support and the connector between the crank and the connecting rod adopt double rolling bearings to decrease the linkage's swinging amplitude, with lubricant

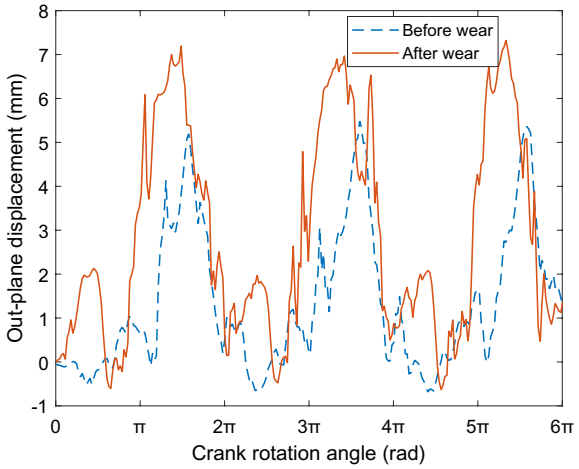

Figure 11 Out-of-plane displacement of journal in 3D joint

to reduce shock and vibration. The spherical joint is also lubricated to reduce resistance during the swinging of the follower. Note that the revolute joint is not lubricated to maintain dry contact, thus accelerating the process of wear. The bearing is fixed upon the connecting rod by the end cover through bolts to facilitate the replacement of sample bearings.

The DIC device is composed of a camera, light source, computer, speckle, image acquisition software, and other parts (seen in Figure 8). The binocular camera measures the out-of-plane displacement. The light source is white luminescence to supplement the illumination intensity on the speckle's measurement surface to enhance the image's definition and contrast ratio. Image acquisition software is developed by ACQTEC Co., Ltd., which can be used for image acquisition and post-processing analysis. The speckle size and speckle density guarantee the best measurement quality for combining the specimen, camera, and lens. Compared with the accelerator measuring approach, the DIC device obtains displacement and vibration information in the full field instead of at just several points. Implementing the digital image correlation method is shown in Figure 9.

The experiment's parameters are shown in Table 3. The material properties are the same as those in the simulation study. The undergoing cycle numbers of wear are 4×10^5 and 1.2×10^6 times under normal temperature. The numbers of revolution cycles are calculated by operating time and rotation speed in the four-bar mechanism. Considering that the wear coefficient is very small and a long-term test is needed to obtain a significant wear amount, more wear cycles are adopted here compared with the

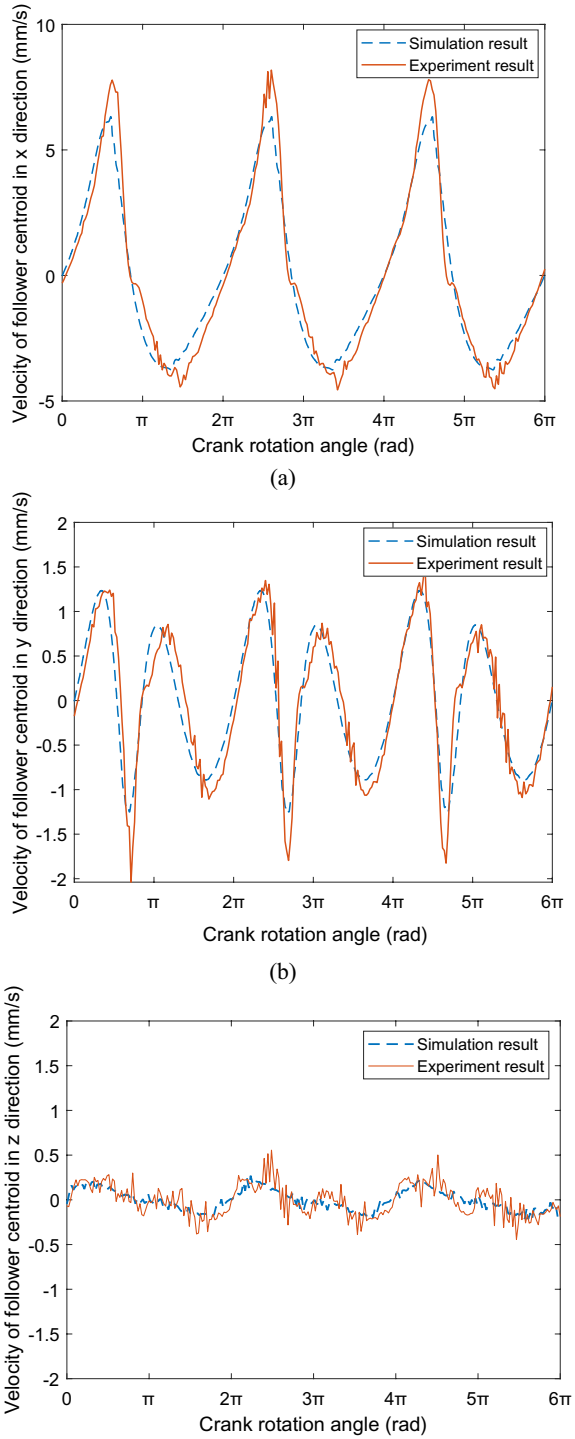

Figure 12 Velocity of follower centroid in simulation and DIC measurement: (**a**) in *x*-direction, (**b**) in *y*-direction, (**c**) in *z*-direction

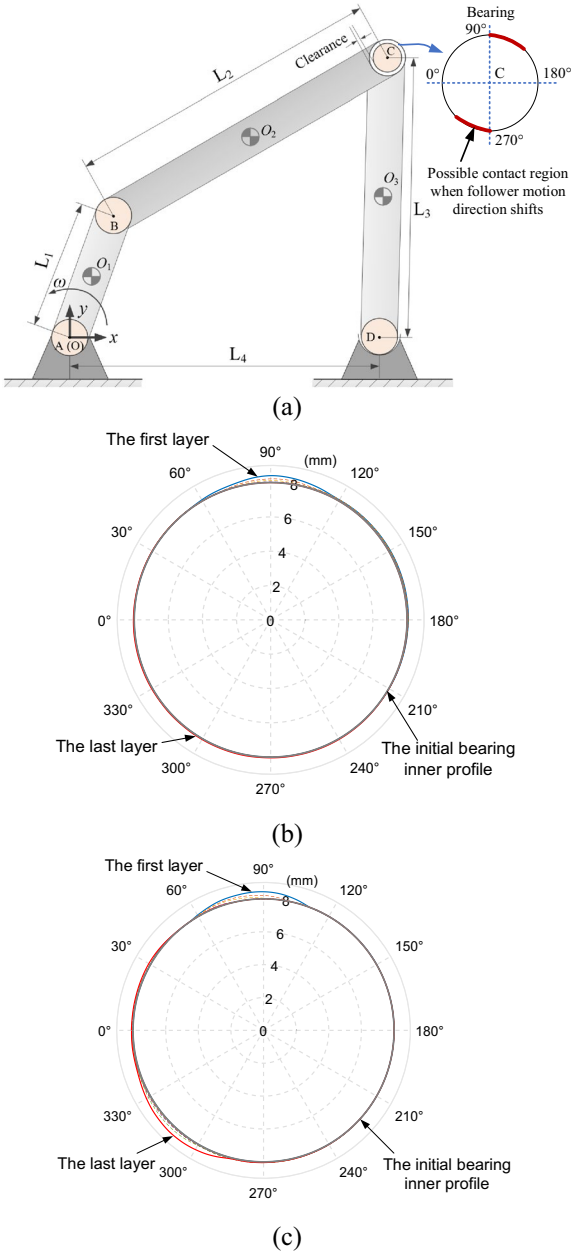

Figure 13 Wear depth distribution on the bearing's inner surface in contour measurement: (**a**) Definition of angular direction on bearing, (**b**) After 4×10^5 wear cycles, (**c**) After 1.2×10^6 wear cycles

simulation study. Alcohol is used to clean the testing bearing in an ultrasonic cleaner before measuring.

The cylindricity measuring machine Talyrond® 565H (manufactured by Taylor Hobson), which provides high-precision surface measurement and analysis, is used to measure the cylindricity and the inner contour of the worn bearing, with a roundness measurement accuracy of 0.03 μm. With the help of this machine, a continuous

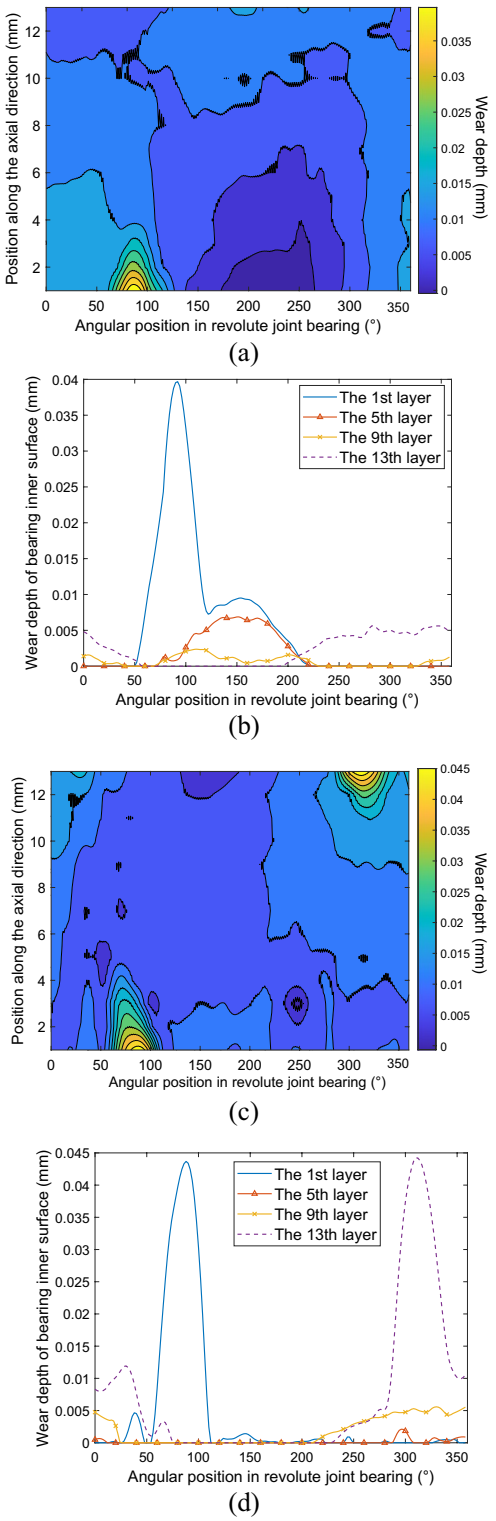

Figure 14 Wear depth distribution for worn bearing: (**a**) Contour plot of bearing's inner surface after 4×10^5 wear cycles, (**b**) Wear depth curves after 4×10^5 wear cycles, (**c**) Contour plot of bearing's inner surface after 1.2×10^6 wear cycles, (**d**) Wear depth curves after 1.2×10^6 wear cycles

dotting test occurs layer by layer along the axial direction at an interval of 1 mm, with a total of 13 testing layers. Figure 10 shows the cylindricity measuring machine and testing bearing before and after wear. The cylindricity values of the bearing's inner surface before wear, after 4×10^5 wear cycles, and after 1.2×10^6 wear cycles and are 5.02 μm, 33.34 μm, and 46.57 μm, respectively. Additionally, an uneven wear region is significantly observed on the inner surface of the worn bearing, which indicates the spatial movement and frequent contact have occurred in the revolute joint.

4.2 Test Results and Discussion

The test results in the four-bar mechanism are presented in this section. Specifically, the mechanism's dynamic performance and the wear depth distribution on the bearing are discussed. Figure 11 shows the out-of-plane displacement curves of the journal before and after wear. Figure 12 shows the comparison of follower centroid's velocity between simulation and experiment results. Figure 13 shows the wear depth distribution on the bearing's inner surface in the contour measurement after different wear cycles. Figure 14 further displays the wear region location with contour plots.

Due to the axial clearance, the journal of a revolute joint exhibits spatial motion trajectories rather than planar ones. This phenomenon is verified in Figure 11, where the out-of-plane displacement of the journal does not equal zero, but varies periodically. Meanwhile, the maximum values of the out-of-plane displacement in the bearing before and after wear are approximately 5.5 mm and 7 mm, which is quite larger than the initial 1 mm axial clearance. This indicates that the two joints on the crank do not move ideally in-plane even though necessary methods have already been taken to prevent the out-of-plane movement here. The out-of-plane displacement of the other linkages could influence the revolute join's motion. Note that the amplitude of the out-of-plane displacement curve after wear is much higher than that of before wear. This is attributed to the progressively enlarged contact profile as well as the revolute joint's clearance after wear. Under the influence of the enlarged clearance, shocks and vibrations in the 3D revolute joint would appear more frequently and significantly.

A comparison of the follower centroid's velocity after wear between simulation and experiment results is shown in Figure 12. Velocity curves of the follower centroid in three directions (i.e., x, y, and z directions) are presented in Figure 12(a), (b), and (c), respectively. It is found that the simulation results are well in line with the experiment results measured by DIC method. Notably, the velocity curves have significant burrs when they reach extremum points. It demonstrates the existence of contacts and impacts at these moments, which could accelerate the wear procedure.

Figure 13 depicts the wear depth distribution on the inner surface of a 16-mm-diameter bearing in contour measurement for 4×10^5 and 1.2×10^6 crank rotation cycles. The definition of the angular direction from 0 to 360° on the bearing is illustrated in Figure 13(a). It shows that the 0° direction on the bearing is parallel to the ground and pointing to the crank when the follower is vertical to the ground. Meanwhile, two possible contact regions on the bearing at the time of the follower motion shift are pointed out. Because the contour measurement is carried out layer by layer at an interval of 1 mm along the axial direction, the testing result for each bearing in Figure 13 has 13 profile layers. The first and last layers are drawn using a continuous line, while the 2nd to 12th layers are drawn using a dotted line. These wear depth curves are exaggerated for a clear illustration.

From the curves of wear depth on the bearing surface, it is obviously apparent that when the wearing procedure undergoes 4×10^5 cycles, the maximum wear depth locates around 90° direction near the first layer; when the wearing procedure undergoes 1.2×10^6 cycles, the maximum wear depth locates around 90° and 310° directions near the first layer and the last layer, respectively. In those areas with significant wear depth, more contacts and impacts would take place. The maximum wear depth's location can be explained by the two possible contact regions on the bearing at the time of the follower motion shift. Note that the wear depth distribution curves in circumstances with 4×10^5 and 1.2×10^6 cycles are not entirely coincident. Also, the final wear depth distribution in the testing result is similar to the simulation result. They compose the evidence of the journal's spatial movement in the 3D revolute joint.

To intuitively present the wear depth distribution on the bearing inner surface, further analysis for the testing result is conducted. From the curves of wear depth on the bearing's inner surface in Figure 14, the wear depth is found near the two bearing edges (namely near the 1st and 13th layers) and tends to be larger than other regions. Moreover, the wear depth distribution in each layer is non-uniform with significant peaks at specific angular locations. The contour plots draw a detailed wear depth distribution on the bearing inner surface. Early wear (4×10^5 cycles) mainly takes place on one side of the bearing, while later period wear (1.2×10^6 cycles) takes place on both sides of the bearing. Additionally, the connecting line for the two wear region centers is not parallel to the bearing's centric line, indicating that a contact mode shift appears in different wear stages.

In general, the experimental results demonstrate the irregular distribution of wear depth in the 3D revolute joint. The wear depth notably is more significant in some specific regions. The location of the maximum wear depth is in line with the simulation results. The measured performance (including out-of-plane displacement) indicates that wear deteriorates the mechanism's dynamic behaviors.

5 Conclusions

This study proposes an approach to integrate the dynamic equation of the 3D revolute clearance joint with the calculation of wear depth. An improved contact force calculation formula based on the L–N model is proposed, which takes the time-varying and nonlinear contact stiffness into account. To validate the proposed model, the DIC measurement and cylindricity test are conducted and the measurement results are compared to the numerical simulation. These simulation and experiment analysis have the following demonstrations:

(1) The nonlinear contact stiffness brings about significant spikes in the contact force calculation. The proposed model that considers time-varying stiffness is more realistic than existing models.
(2) The out-of-plane motion of the journal in the revolute joint is observed in DIC measurement. The cylindricity values of bearing inner surface before wear, after 4×10^5 wear cycles, and after 1.2×10^6 wear cycles and are 5.02 μm, 33.34 μm, and 46.57 μm, respectively. These results indicate that the geometrical profile of the bearing in the revolute joint is significantly changed after wear.
(3) The maximum wear depth locates around 90° and 310° directions after 1.2×10^6 wear cycles near the first layer and the last layer, respectively. The location of the maximum wear depth can be explained by the two possible contact regions on the bearing at the time of follower motion shifts.
(4) The wear amount distribution on the bearing's inner surface is uneven in the axial and radial directions. The wear depth near the two bearing edges tends to be larger than in other regions.

This study theoretically presents an effective method in wear prediction in the 3D revolute joint that considers time-varying contact stiffness. This work also helps to understand the wear-prone parts of the revolute joint and enhance its durability and reliability through an improved design. The future work will focus on the effects of other factors (i.e., different clearance sizes, lubrication, rotation speed, load condition, etc.) on the dynamic performance of mechanical systems.

Acknowledgements
The authors sincerely thanks to the anonymous reviewers for their insightful comments and suggestions.

Authors' Contributions
LZ wrote the manuscript, performed the experiment and analyses; YF contributed to data analysis and manuscript preparation; GB helped perform the analysis with constructive discussions; JT discussed the results and revised the manuscript. All authors read and approved the final manuscript.

Authors' Information
Li Zhang, born in 1993, is currently a lecturer at *College of Information and Communication, National University of Defense Technology, China*. He received his PhD degree from *National University of Defense Technology, China*, in 2022. His research interests include dynamic modeling, prognostic and health management, reliability test and evaluation.
Yining Fang, born in 1991, is currently a lecturer at *Laboratory of Science and Technology on Integrated Logistics Support, College of Intelligence Science and Technology, National University of Defense Technology, China*. She received her PhD degree from *University of Alberta, Canada*, in 2019. Her research interests include modeling and identification for complex systems.
Guanghan Bai, born in 1986, is currently an associate professor at *Laboratory of Science and Technology on Integrated Logistics Support, College of Intelligence Science and Technology, National University of Defense Technology, China*. He received his PhD degree from *University of Alberta, Canada*, in 2016. His research interests include system reliability and resilience.
Junyong Tao, born in 1969, is currently a professor at *Laboratory of Science and Technology on Integrated Logistics Support, College of Intelligence Science and Technology, National University of Defense Technology, China*. He received his PhD degree from *National University of Defense Technology, China*, in 2000. His research interests include system reliability and fault diagnosis.

Funding
Not applicable.

Declarations

Competing Interests
The authors declare no competing financial interests.

Received: 4 June 2021 Revised: 15 July 2022 Accepted: 13 September 2023
Published online: 17 November 2023

References

[1] Q Tian, P Flores, H M Lankarani. A comprehensive survey of the analytical, numerical and experimental methodologies for dynamics of multibody mechanical systems with clearance or imperfect joints. *Mechanism and Machine Theory*, 2018, 122: 1–57.
[2] Z F Bai, Y Sun. A study on dynamics of planar multibody mechanical systems with multiple revolute clearance joints. *European Journal of Mechanics - A/Solids*, 2016, 60: 95–111.
[3] X Lai, Q Lai, H Huang, et al. New approach to assess and rank the impact of revolute joint wear on the kinematic accuracy in the low-velocity planar mechanism. *Advances in Engineering Software*, 2016, 102: 71–82.
[4] S Erkaya, İ Uzmay. Investigation on effect of joint clearance on dynamics of four-bar mechanism. *Nonlinear Dynamics*, 2009, 58(1–2): 179.
[5] P Li, W Chen, D Li, et al. A novel transition model for lubricated revolute joints in planar multibody systems. *Multibody System Dynamics*, 2016, 36(3): 279–294.

[6] P Li, W Chen, D Li, et al. Wear analysis of two revolute joints with clearance in multibody systems. *Journal of Computational and Nonlinear Dynamics*, 2016, 11(1): 1–7.

[7] Y Li, G Chen, D Sun, et al. Dynamic analysis and optimization design of a planar slider–crank mechanism with flexible components and two clearance joints. *Mechanism and Machine Theory*, 2016, 99: 37–57.

[8] W Xiang, S Yan, J Wu, et al. Dynamic response and sensitivity analysis for mechanical systems with clearance joints and parameter uncertainties using Chebyshev polynomials method. *Mechanical Systems and Signal Processing*, 2020, 138: 106596.

[9] P Flores, J Ambrósio, J C P Claro, et al. Spatial revolute joints with clearances for dynamic analysis of multi-body systems. *Proceedings of the Institution of Mechanical Engineers, Part K: Journal of Multi-body Dynamics*, 2006, 220(4): 257–271.

[10] Q Tian, C Liu, M Machado, et al. A new model for dry and lubricated cylindrical joints with clearance in spatial flexible multibody systems. *Nonlinear Dynamics*, 2011, 64(1): 25–47.

[11] C Liu, Q Tian, H Hu. Dynamics and control of a spatial rigid-flexible multibody system with multiple cylindrical clearance joints. *Mechanism and Machine Theory*, 2012, 52: 106–129.

[12] S Yan, W Xiang, L Zhang. A comprehensive model for 3D revolute joints with clearances in mechanical systems. *Nonlinear Dynamics*, 2015, 80(1): 309–328.

[13] N Akhadkar, V Acary, B Brogliato. Multibody systems with 3D revolute joints with clearances: an industrial case study with an experimental validation. *Multibody System Dynamics*, 2018, 42(3): 249–282.

[14] K Chen, G Zhang, H Wang, et al. Numerical and experimental investigations on dynamic response of hydraulic cylinder with 3D spatial joints considering radial and axial clearances. *Shock and Vibration*, 2019, 2019(3): 1–24.

[15] Z F Bai, J Zhao. A study on dynamic characteristics of satellite antenna system considering 3D revolute clearance joint. *International Journal of Aerospace Engineering*, 2020, 2020(4): 1–15.

[16] F Marques, F Isaac, N Dourado, et al. An enhanced formulation to model spatial revolute joints with radial and axial clearances. *Mechanism & Machine Theory*, 2017, 116: 123–144.

[17] P Flores. Modeling and simulation of wear in revolute clearance joints in multibody systems. *Mechanism and Machine Theory*, 2009, 44(6): 1211–1222.

[18] L X Xu, Y C Han, Q B Dong, et al. An approach for modelling a clearance revolute joint with a constantly updating wear profile in a multibody system: simulation and experiment. *Multibody System Dynamics*, 2018: 1–22.

[19] J Ma, G Chen, L Ji, et al. A general methodology to establish the contact force model for complex contacting surfaces. *Mechanical Systems and Signal Processing*, 2020, 140: 106678.

[20] B Zhao, Z N Zhang, X D Dai. Modeling and prediction of wear at revolute clearance joints in flexible multibody systems. *Proceedings of the Institution of Mechanical Engineers, Part C: Journal of Mechanical Engineering Science*, 2014, 228(2): 317–329.

[21] S Mukras, N A Mauntler, N H Kim, et al. Modeling a slider-crank mechanism with joint wear. *SAE International Journal of Passenger Cars-Mechanical Systems*, 2009, 2(1): 600–612.

[22] S Mukras, N Mauntler, N H Kim, et al. Dynamic modeling of a slider-crank mechanism under joint wear. *Proceedings of the ASME 2008 International Design Engineering Technical Conferences and Computers and Information in Engineering Conference*, 2008, American Society of Mechanical Engineers.

[23] S Mukras, N H Kim, N A Mauntler, et al. Analysis of planar multibody systems with revolute joint wear. *Wear*, 2010, 268(5): 643–652.

[24] B Zhao, X D Dai, Z N Zhang, et al. Numerical study of parametric effects on joint wear in the flexible multibody systems with different flexibilities and clearance sizes. *Proceedings of the Institution of Mechanical Engineers, Part J: Journal of Engineering Tribology*, 2014, 228(8): 819–835.

[25] Z F Bai, Y Zhao, X Wang. Wear analysis of revolute joints with clearance in multibody systems. *Science China Physics, Mechanics and Astronomy*, 2013, 56(8): 1581–1590.

[26] W Xiang, S Yan, J Wu. A comprehensive method for joint wear prediction in planar mechanical systems with clearances considering complex contact conditions. *Science China Technological Sciences*, 2015, 58(1): 86–96.

[27] J M You, T N Chen. Estimation for normal parameters of joint surfaces based on fractal theory. *Journal of Shanghai Jiaotong University*, 2011, 45(9): 1275–1280.

[28] H Yang. Calculation model of the normal contact stiffness of joints based on the fractal geometry and contact theory. *Journal of Mechanical Engineering*, 2013, 49 (1): 102–107.

[29] Q Sun, X Liu, X Mu, et al. Estimation for normal contact stiffness of joint surfaces by considering the variation of critical deformation. *Assembly Automation*, 2020, 40: 399–406.

[30] X Wang, G Liu, S Ma, et al. Study on dynamic responses of planar multibody systems with dry revolute clearance joint: Numerical and experimental approaches. *Journal of Sound and Vibration*, 2019, 438: 116–138.

[31] M Babaeeian, M Mohammadimehr. Investigation of the time elapsed effect on residual stress measurement in a composite plate by DIC method. *Optics and Lasers in Engineering*, 2020, 128: 106002.

[32] L Benabou, T A Nguyen-Van, Q B Tao, et al. Methodology for DIC-based evaluation of the fracture behaviour of solder materials under monotonic and creep loadings. *Engineering Fracture Mechanics*, 2020, 239: 107285.

[33] M Babaeeian, M Mohammadimehr. Experimental and computational analyses on residual stress of composite plate using DIC and Hole-drilling methods based on Mohr's circle and considering the time effect. *Optics and Lasers in Engineering*, 2021, 137: 106355.

[34] P Flores, J Ambrósio, J C P Claro, et al. Dynamic behaviour of planar rigid multi-body systems including revolute joints with clearance. *Proceedings of the Institution of Mechanical Engineers, Part K: Journal of Multi-body Dynamics*, 2007, 221(2): 161–174.

[35] P Flores, R Leine, C Glocker. Modeling and analysis of planar rigid multibody systems with translational clearance joints based on the non-smooth dynamics approach. *Multibody System Dynamics*, 2010, 23(2): 165–190.

[36] S Mukras, N H Kim, N A Mauntler, et al. Comparison between elastic foundation and contact force models in wear analysis of planar multibody system. *Journal of Tribology*, 2010, 132(3): 1–11.

[37] Z F Bai, Y Zhao. A hybrid contact force model of revolute joint with clearance for planar mechanical systems. *International Journal of Non-Linear Mechanics*, 2013, 48: 15–36.

[38] Z F Bai, Y Zhao, J Chen. Dynamics analysis of planar mechanical system considering revolute clearance joint wear. *Tribology International*, 2013, 64: 85–95.

[39] V L Reis, G B Daniel, K L Cavalca. Dynamic analysis of a lubricated planar slider–crank mechanism considering friction and Hertz contact effects. *Mechanism and Machine Theory*, 2014, 74: 257–273.

[40] Y Chen, Y Sun, C Chen. Dynamic analysis of a planar slider-crank mechanism with clearance for a high speed and heavy load press system. *Mechanism and Machine Theory*, 2016, 98: 81–100.

[41] D Sun, G Chen. Kinematic accuracy analysis of planar mechanisms with clearance involving random and epistemic uncertainty. *European Journal of Mechanics-A/Solids*, 2016, 58: 256–261.

[42] B Zhao, Z N Zhang, C C Fang, et al. Modeling and analysis of planar multibody system with mixed lubricated revolute joint. *Tribology International*, 2016, 98: 229–241.

[43] B Zhao, K Zhou, Y B Xie. A new numerical method for planar multibody system with mixed lubricated revolute joint. *International Journal of Mechanical Sciences*, 2016, 113: 105–119.

[44] S B Farahan, M R Ghazavi, S Rahmanian. Bifurcation in a planar four-bar mechanism with revolute clearance joint. *Nonlinear Dynamics*, 2017, 87(2): 955–973.

[45] G Wang, Z Qi, J Wang. A differential approach for modeling revolute clearance joints in planar rigid multibody systems. *Multibody System Dynamics*, 2017, 39(4): 311–335.

[46] A Zhu, S He, J Zhao, et al. A nonlinear contact pressure distribution model for wear calculation of planar revolute joint with clearance. *Nonlinear Dynamics*, 2017, 88(1): 315–328.

[47] Z F Bai, J J Zhao, J Chen, et al. Design optimization of dual-axis driving mechanism for satellite antenna with two planar revolute clearance joints. *Acta Astronautica*, 2018, 144: 80–89.

[48] X Tan, G Chen, D Sun, et al. Dynamic analysis of planar mechanical systems with clearance joint based on LuGre friction model. *Journal of Computational and Nonlinear Dynamics*, 2018, 13(6): 1537–1545.

[49] Y Li, C Wang, W Huang. Dynamics analysis of planar rigid-flexible coupling deployable solar array system with multiple revolute clearance joints. *Mechanical Systems and Signal Processing*, 2019, 117: 188–209.
[50] X Wang, W Lin, X Ji, et al. Dynamic analysis of a planar multibody system with multiple revolute clearance joints. *Proceedings of the Institution of Mechanical Engineers, Part C: Journal of Mechanical Engineering Science*, 2019, 233: 3429–3443.
[51] E Zheng, T Wang, J Guo, et al. Dynamic modeling and error analysis of planar flexible multilink mechanism with clearance and spindle-bearing structure. *Mechanism and Machine Theory*, 2019, 131: 234–260.
[52] F J Cavalieri, A Cardona. Non-smooth model of a frictionless and dry three-dimensional revolute joint with clearance for multibody system dynamics. *Mechanism and Machine Theory*, 2018, 121: 335–354.
[53] H M Lankarani, P E Nikravesh. A contact force model with hysteresis damping for impact analysis of multibody systems. *Journal of Mechanical Design*, 1990, 112(3): 369–376.
[54] S Mukras, N H Kim, W G Sawyer, et al. Numerical integration schemes and parallel computation for wear prediction using finite element method. *Wear*, 2009, 266(7): 822–831.
[55] X Lai, H He, Q Lai, et al. Computational prediction and experimental validation of revolute joint clearance wear in the low-velocity planar mechanism. *Mechanical Systems and Signal Processing*, 2017, 85: 963–976.
[56] J Baumgarte. Stabilization of constraints and integrals of motion in dynamical systems. *Computer Methods in Applied Mechanics and Engineering*, 1972, 1(1): 1–16.
[57] B Zhao, Z N Zhang, X D Dai. Prediction of wear at revolute clearance joints in flexible mechanical systems. *Procedia Engineering*, 2013, 68: 661–667.
[58] Z F Bai, H B Zhang, Y Sun. Wear prediction for dry revolute joint with clearance in multibody system by integrating dynamics model and wear model. *Latin American Journal of Solids and Structures*, 2014, 11: 2624–2647.